

## Article

# Study on the Evolution of the $\gamma'$ Phase and Grain Boundaries in Nickel-Based Superalloy during Interrupted Continuous Cooling

Haiping Wang <sup>1,\*</sup>, Dong Liu <sup>1</sup>, Jianguo Wang <sup>1,\*</sup>, Yanhui Yang <sup>1</sup>, Haodong Rao <sup>1</sup>, Hai Wang <sup>1</sup>, Jungang Nan <sup>1</sup> and Longxiang Wang <sup>2</sup>

<sup>1</sup> State Key Laboratory of Solidification Processing, Northwestern Polytechnical University, Xi'an 710072, China; liudong@nwpu.edu.cn (D.L.); YhYang@nwpu.edu.cn (Y.Y.); rhd@mail.nwpu.edu.cn (H.R.); whai@mail.nwpu.edu.cn (H.W.); JungangNan@mail.nwpu.edu.cn (J.N.)  
<sup>2</sup> Avic Heavy Machinery Co., Ltd., Guizhou 520100, China; lxWang@163.com  
\* Correspondence: whp0604@mail.nwpu.edu.cn (H.W.); jianguow@nwpu.edu.cn (J.W.)

**Abstract:** The formation of the irregular  $\gamma'$  precipitates in the nickel-based superalloy Waspaloy was investigated during the continuous cooling, which is relevant to the cooling rates and interrupted temperature. The morphology of the  $\gamma'$  precipitates was observed to change from a dispersed sphere to the flower-like one with the decreasing of the cooling rates. It was found that there are three modes of transportation of the solute atoms involved in relation to the  $\gamma'$  precipitates: dissolution from the small  $\gamma'$  precipitates to the  $\gamma$  matrix, diffusion to the large  $\gamma'$  precipitates from the matrix, and the short distance among  $\gamma'$  precipitates close to each other. Meanwhile, the slower cooling rates tend to result in the serrated grain boundaries, and the wavelength between successive peaks ( $\lambda$ ) and the maximum amplitude ( $A$ ) are larger with the decreasing of the cooling rates. The content of the low  $\Sigma$ CSL boundaries increases with the decreasing of the cooling rates, which is of great benefit in improving the creep property of the Waspaloy.

**Keywords:** Waspaloy; continuous cooling;  $\gamma'$  precipitates; serrated grain boundaries; creep property



**Citation:** Wang, H.; Liu, D.; Wang, J.; Yang, Y.; Rao, H.; Wang, H.; Nan, J.; Wang, L. Study on the Evolution of the  $\gamma'$  Phase and Grain Boundaries in Nickel-Based Superalloy during Interrupted Continuous Cooling. *Crystals* **2021**, *11*, 1464. <https://doi.org/10.3390/cryst11121464>

Academic Editor: Hongbiao Dong

Received: 24 October 2021  
Accepted: 24 November 2021  
Published: 26 November 2021

**Publisher's Note:** MDPI stays neutral with regard to jurisdictional claims in published maps and institutional affiliations.



**Copyright:** © 2021 by the authors. Licensee MDPI, Basel, Switzerland. This article is an open access article distributed under the terms and conditions of the Creative Commons Attribution (CC BY) license (<https://creativecommons.org/licenses/by/4.0/>).

## 1. Introduction

Waspaloy is widely used in high-temperature applications, such as turbine disks and blades, as well as the nonrotation high-temperature structural parts, such as aero engine casing and rotating parts. It is mainly because of the excellent tensile strength and rupture strength below 760 °C, along with the enhanced oxidation resistance below 870 °C [1–4]. Generally, the microstructure of Waspaloy consists of the disordered face-centered cubic matrix  $\gamma$  phase, carbides (mainly the precipitated  $M_{23}C_6$  during aging), and the dispersed L1<sub>2</sub>-ordered  $\gamma'$  precipitates (Ni<sub>3</sub>(Ti, Al)) (precipitated during solution treatment and aging) [5–8]. In addition, the excellent properties of Waspaloy depend on the  $\gamma'$  precipitate. Previous studies [9,10] have noted that the morphology, size, distribution, and volume fraction can influence the mechanical properties. In order to determine this effect, it is necessary to investigate the factors that influence the evolution of the  $\gamma'$  precipitates.

The size, distribution, and volume fraction of the  $\gamma'$  precipitates of superalloys, and even the Waspaloy, have already been investigated [10–14]. However, the morphology of the  $\gamma'$  precipitates has not been reported in Waspaloy. The precipitation and growth of  $\gamma'$  precipitates cooling from high temperature to low temperature (below the absolute dissolution temperature of the  $\gamma'$  precipitates) are rather complicated processes. The cooling rates are considered to influence the morphology of the  $\gamma'$  precipitates. When the cooling rate is fast, such as water quenching, the morphology of the  $\gamma'$  precipitates tends to form the single spherical morphology and is prone to showing high density [15]. Besides, the higher cooling rates are usually accompanied by the straight grain boundaries, because it maintains the microstructure at the high temperature and there is nearly no time for the

variation. When the cooling rate slows down, it has more time for the process of precipitation and growth and the morphology of the  $\gamma'$  precipitates tends to form two or more different sizes, even the irregular-shaped and fan-type  $\gamma'$  precipitates. Correspondingly, the lower cooling rate often leads to the formation of serrated grain boundaries [11,16,17], which is due to the presence of the heterogeneous phases at the grain boundaries [18].

In this paper, the morphology of the  $\gamma'$  precipitates under different cooling rates and interrupted cooling from high temperature were investigated. The relationship between the morphology and the cooling rates was obtained, and this illustrated the formation process of the flower-like  $\gamma'$  precipitates during the continuous cooling. In addition, the influence of the cooling rate on the serrated grain boundaries and low  $\Sigma$ CSL boundaries was studied.

## 2. Materials and Experiment

The material used in this paper is the two-phase ( $\gamma$ - $\gamma'$ ) nickel-based superalloy Waspaloy in the form of wrought bar with the diameter of 314 mm and height of 60 mm, which is the usual state before disk forging, and was provided by Baoshan Iron & Steel Co., Ltd. in China. The chemical compositions of Waspaloy are shown in Table 1. The microstructure of the as-received state is shown in Figure 1, which is composed of the coarse equiaxed grains of the  $\gamma$  phase (face-centered cubic (fcc) solid solution) and the two scales of the  $\gamma'$  precipitates ( $\text{Ni}_3(\text{Al,Ti})$ , ordered  $L1_2$  cubic structure). The two scales of  $\gamma'$  precipitates were formed during the heat treatment at subsolvus temperature ( $T_{\text{sub}}$ ) and aging treatment.

**Table 1.** The chemical composition of the Waspaloy.

Elements	Al	Ti	Co	Cr	Mo	C	Ni
Wt %	1.46	3.18	13.9	19.15	4.75	0.05	Bal.

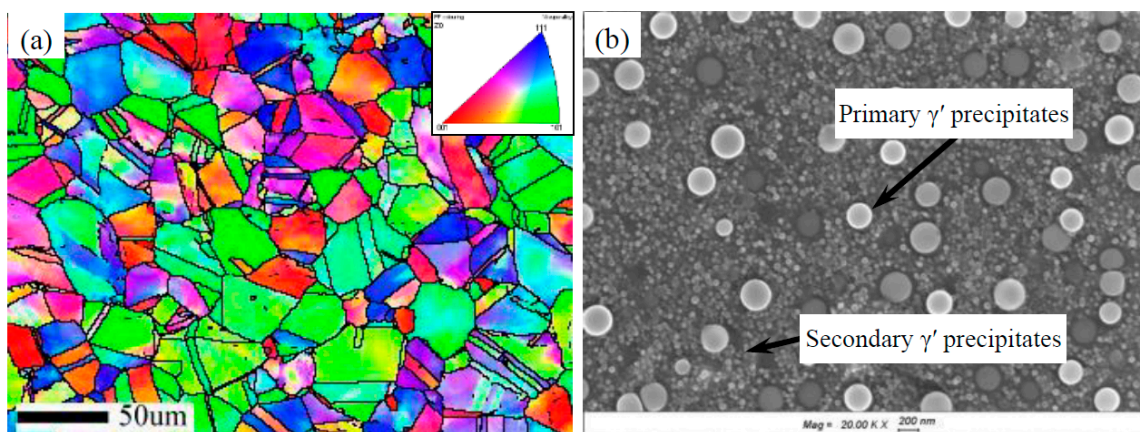


**Figure 1.** The initial microstructure of the specimen from the wrought bar: (a) IPF map showing the homogeneous grains; (b) SEM map showing the duplex-sized spherical  $\gamma'$  precipitates.

The wrought bar underwent the typical heat treatment of 1030 °C for 4 h, was air cooled (AC), followed by a stabilization period at 845 °C for 4 h (AC), and then aged at 760 °C for 16 h (AC). Figure 1a shows the EBSD characterization of the specimen from the wrought bar, from which it can be concluded that the grain size is homogeneous, with the average grain size of 46  $\mu\text{m}$  (ASTM6) in diameter. Figure 1b exhibits the SEM characterization of the sample from the wrought bar. It reveals that the duplex-sized spherical  $\gamma'$  precipitates are uniformly distributed in the  $\gamma$  matrix, and the average diameter of the  $\gamma'$  precipitates is 262 nm and 43 nm, respectively.

The wrought bar has been subjected to a series of deformation and heat treatment to obtain the stable microstructure. In the process of deformation, due to the inhomogeneity

of deformation and nonuniform strain distribution, there are different strain distributions in different positions of the wrought bar. Meanwhile, there are some other factors that can influence the experimental results, such as composition segregation and so on. Accordingly, it was machined into the small cubic metallographic specimens with the edge length of 10 mm on the 1/2 radius of the wrought bar by wire electrical discharge machining (WEDM).

All the specimens from the wrought bar were processed at the supersolvus solution temperature ( $T_{\text{sup}}$ ) of 1080 °C to obtain the fully solute state. Grain growth takes place and the grain boundaries are expected to be straight. Continuous cooling was followed after holding at the  $T_{\text{sup}}$  for 30 min. The specimens were cooled at the rate of 20 °C/min, 10 °C/min, 5 °C, 2.5 °C/min, 1 °C/min, 0.5 °C/min, 0.25 °C/min, and water quenched, respectively. In order to study the influence of the interrupted temperature, the interrupted cooling experiments were carried out at each continuous cooling process. Each cooling was interrupted at different intermediate temperatures and was interrupted at 1000 °C, 950 °C, 900 °C, 850 °C, 800 °C, and 20 °C. Accordingly, the interrupted cooling specimens were taken out immediately and water quenched to maintain the high-temperature microstructures. In order to ensure the reliability of the experiment, two samples were prepared under each experimental condition. The temperature control of the entire process of continuous cooling was maintained to within  $\pm 1$  °C using a calibrated N-type thermocouple attached to the sample surface.

Scanning electron microscopy (SEM) and electron backscatter diffraction (EBSD) samples were prepared by mechanical grinding and standard metallographic polishing techniques, and then the samples were electrolytically polished at 20 V for 10 s and electrolytically etched at 10 V for 10 s at room temperature using a DC voltage. The solution of the electrolytic polishing is 20%  $\text{H}_2\text{SO}_4$  and 80%  $\text{CH}_3\text{OH}$ , and the solution of electrochemically etching is 10 mL  $\text{H}_2\text{SO}_4$ , 150 mL  $\text{H}_3\text{PO}_4$  and 15 g  $\text{CrO}_3$ . The samples were examined with a scanning electron microscope (Zeiss Gemini 500) at the acceleration voltage of 10 kV, and the magnification was from 10 k times to 50 k times. The equivalent diameter and size distribution of the  $\gamma'$  precipitates were measured from SEM micrographs using the commercial image-analysis software application Image-Pro Plus 6.0. In order to ensure the measurement reliability under each experimental condition, three micrographs under the same condition were measured.

### 3. Results and Discussion

#### 3.1. The Morphology of the $\gamma'$ Precipitates under Different Cooling Rates

Figure 2 shows the SEM micrographs of the primary  $\gamma'$  precipitates under continuous cooling from 1080 °C to room temperature (RT) at different cooling rates. It exhibits that the  $\gamma'$  precipitates were randomly and homogeneously distributed throughout the  $\gamma$  matrix. It can be obtained from Figure 2a that the  $\gamma'$  precipitates have been entirely dissolved into the  $\gamma$  matrix when heat treated at the temperature of 1080 °C and water quenched to RT. When the cooling rate exceeds to 20 °C/min and 10 °C/min, the primary  $\gamma'$  precipitates exhibit monomodal size distribution with a spherical morphology and were very close to each other, many of them even in contact with each other (see the red loops in Figure 2c). It can also be obtained that the diameter of the  $\gamma'$  precipitates is larger with the decreasing of the cooling rate, as the diffusion process is longer with the decreasing of the cooling rates. For instance, the diameter of the  $\gamma'$  precipitates increase from 89.5 nm to 163 nm with the decreasing cooling rates from 20 °C/min to 10 °C/min.

Figure 2d–f presents the  $\gamma'$  precipitates at the cooling rates lower than 10 °C/min. It can be seen that the morphology of the  $\gamma'$  precipitates exhibits the multimodal size distribution and changes from the spherical to the irregular flower-like one. Meanwhile, there are a few  $\gamma'$  precipitates exhibiting spherical morphology (see the red arrows in Figure 2d–f), which is due to the fact that the spherical  $\gamma'$  precipitates may nucleate in a certain region far from the flower-like  $\gamma'$  precipitates. Many of the  $\gamma'$  precipitates were also observed to outline the flower-like one (see the yellow loops in Figure 2d–f). Some

scholars [19,20] indicated that the spherical one was split from the flower-like  $\gamma'$  precipitates in other alloys, which was different from our alloy in this paper, and it will be discussed in the following part. With the decrease in the cooling rate, an increase in the primary  $\gamma'$  precipitates can be observed and the shapes of the  $\gamma'$  precipitates become more and more irregular.

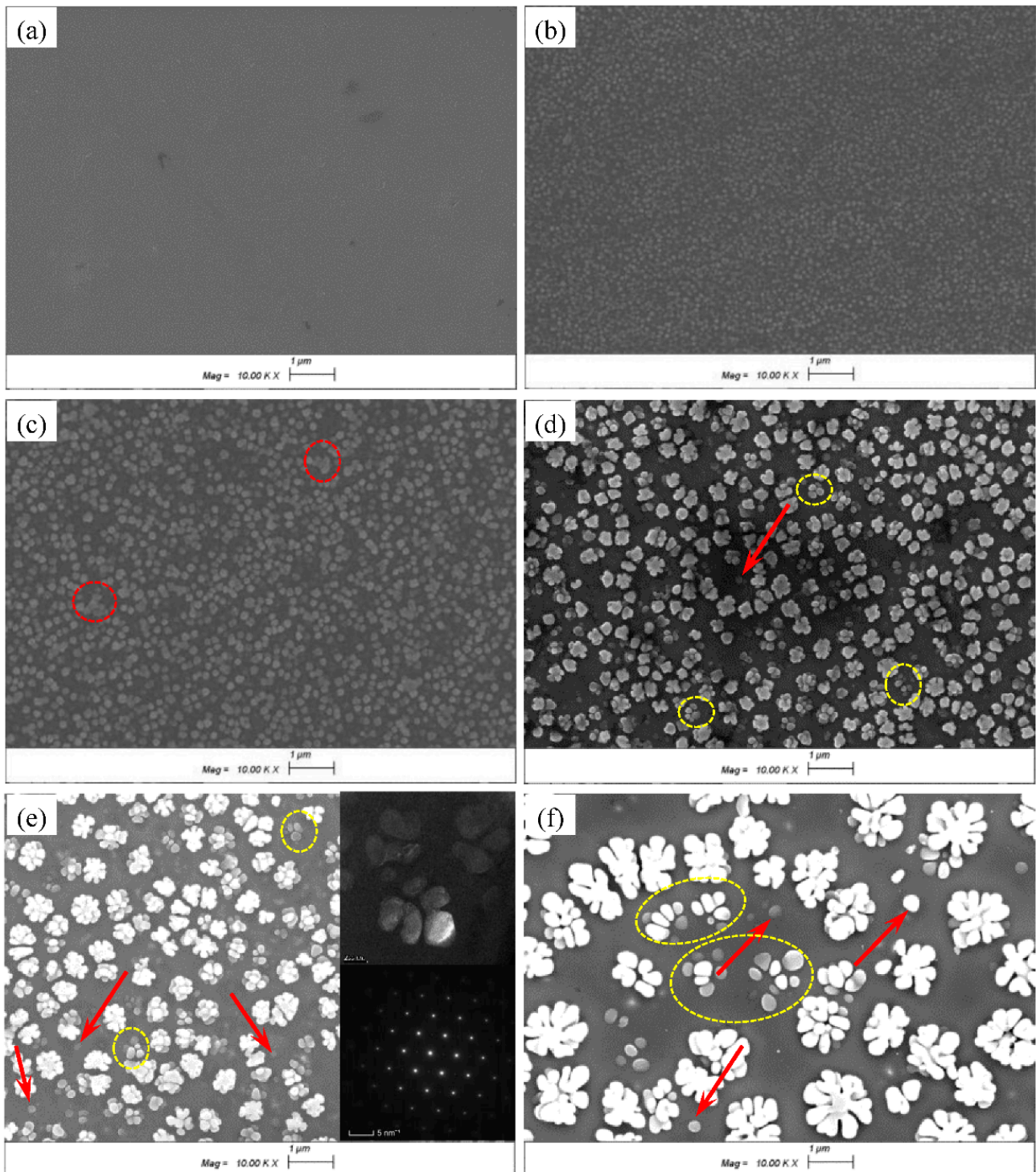


**Figure 2.** The evolution of the  $\gamma'$  precipitates under different cooling rates. (a) Water quenched, (b) 20 °C/min, (c) 10 °C/min, (d) 5 °C/min, (e) 1 °C/min, and (f) 0.25 °C/min.

The transmission electron microscopy (TEM) result was inserted in Figure 2c (top right corner). It shows that the precipitates exhibit the flower-like morphology. The selected area electron diffraction (SAD) pattern was obtained from the region and was also inserted in the inset of Figure 2c (bottom right corner). The SAD pattern confirmed that precipitates are the same FCC structure as the matrix, and the precipitates are the  $\gamma'$  precipitates rather than new phase.

Figure 3 illustrates the effect of the cooling rates on the morphology of the primary  $\gamma'$  precipitates. It shows that the morphology changes from the spherical to irregular-shaped flower-like one. For all the different cooling rates, the volume free energy ( $\Delta G_V$ ) of the  $\gamma'$  precipitates continues to increase for the increasing undercooling when temperatures are below the  $T_{sup}$ , and the nucleation of the  $\gamma'$  precipitates takes place when the  $\Delta G_V$  increase to the critical nucleation barrier. In the case of water cooling, the nucleation and growing of the  $\gamma'$  precipitates almost impossibly took place, because the undercooling is too large. When the cooling rates decrease to 20 °C/min, the nucleation of the  $\gamma'$  precipitates takes place and the high nucleation rate causes the high volume fraction of the  $\gamma'$  precipitates, which can be seen from Figure 2b. Meanwhile, during the fast cooling process, the higher undercooling can limit the diffusion process of the alloy elements consisting of the  $\gamma'$  precipitates. It would restrict the growth of the  $\gamma'$  precipitates, causing the  $\gamma'$  precipitates to keep the spherical morphology. In spite of the nonequilibrium conditions, the high cooling rate also prevents any further nucleation events. Therefore, the monomodal size distribution of spherical  $\gamma'$  precipitates is observed during the fast cooling process. When the cooling rate decreases to 5 °C/min, the whole cooling process contains the nucleation and growth process of the  $\gamma'$  precipitates, where the diffusion process is relatively long, which contributes to the growth of the  $\gamma'$  precipitates. At lower cooling rates, the shape of the  $\gamma'$  precipitates tends to be more cuboidal, which can be attributed to the rapidly increasing coherent strain energy with the growth and accompanying coarsening process [21]. The evolution of the  $\gamma'$  precipitates of Waspaloy during continuous cooling was similar to the other superalloy. Singh et al. [22] and Tiley et al. [23] present the evolution of the  $\gamma'$  precipitates under three kinds of cooling rates, namely water quenching, air cooling, and furnace cooling. They present that the fast cooling, such as water cooling, can precipitate the spherical  $\gamma'$  precipitates, while the slow cooling, such as furnace, can precipitate the flower-like  $\gamma'$  precipitates.

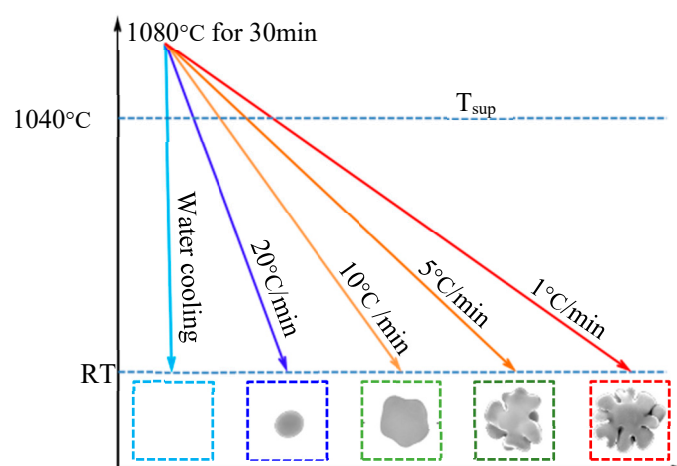


**Figure 3.** Schematic illustration of the effects of the cooling rates on the morphology of the  $\gamma'$  phase.

In order to investigate the size and distribution of the primary  $\gamma'$  precipitates under different cooling rates, Figure 4 shows the particle size frequency distribution of the equivalent diameter of the  $\gamma'$  precipitates. It can be obtained from Figure 4 that an obvious increase in the equivalent diameter with the decreasing of the cooling rates is shown. For instance, the equivalent diameter of the primary  $\gamma'$  precipitates ranges from 700 nm

to 1800 nm when the cooling rate is 0.25 °C/min, while the equivalent diameter of the primary  $\gamma'$  precipitates ranges from 100 nm to 220 nm when the cooling rate is 10 °C/min. Meanwhile, the equivalent diameter of the primary  $\gamma'$  precipitates shows a wider spread with the decrease in the cooling rate, which owes to the irregular and the non-spherical morphology of the primary  $\gamma'$  precipitates. In addition, it can be proved from Figure 2 that the primary  $\gamma'$  precipitates show spherical morphology (Figure 2b) under the cooling rate of 20 °C/min, while showing flower-like morphology (Figure 2f) at the cooling rate of 0.25 °C/min.

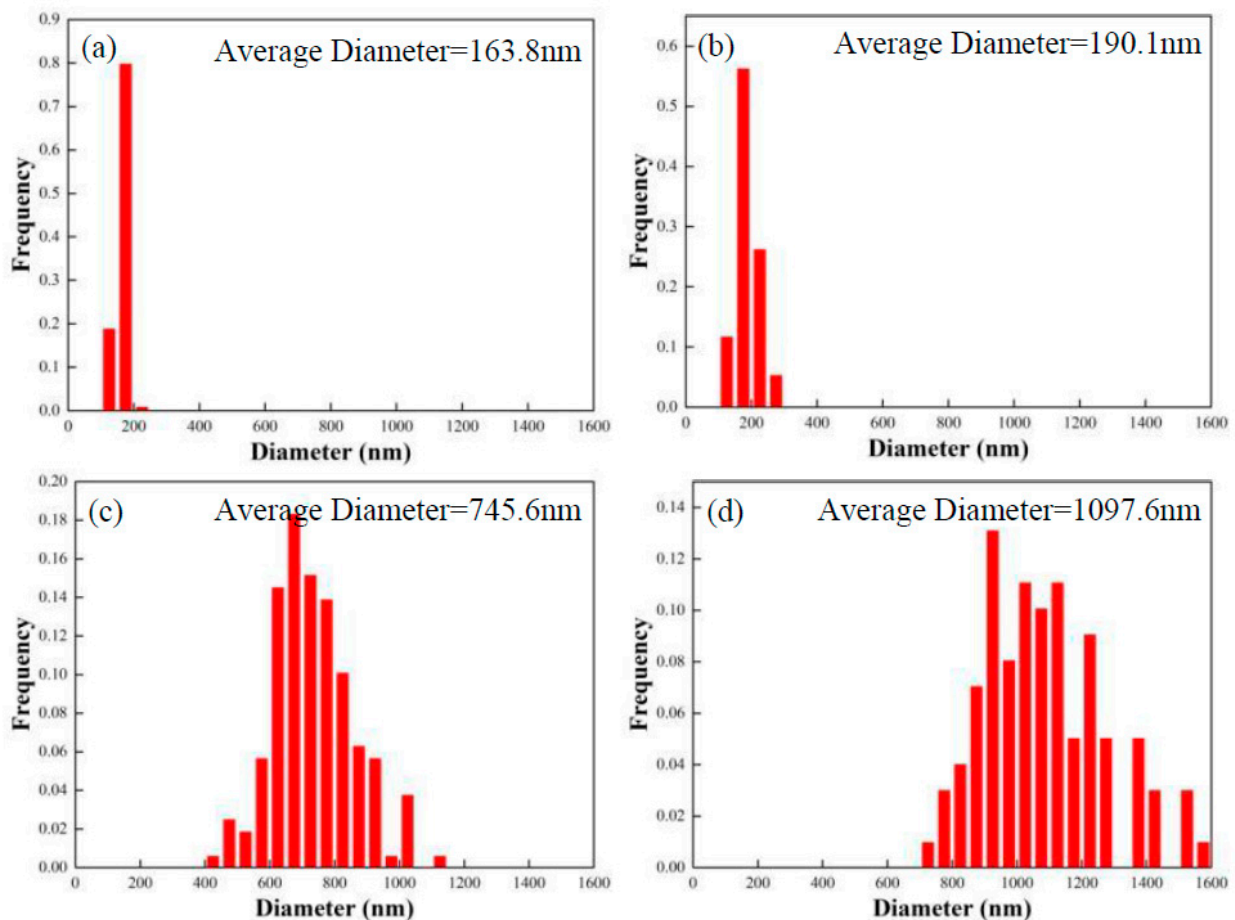


**Figure 4.** The particle size distribution of the primary  $\gamma'$  precipitates under different cooling rates: (a) 10 °C/min, (b) 5 °C/min, (c) 1 °C/min, (d) 0.25 °C/min.

### 3.2. The Morphology of the $\gamma'$ Precipitates at Different Interrupt Temperatures

Figure 5 shows the nucleation and morphological evolution of  $\gamma'$  precipitates during slow cooling from 1080 °C at the cooling rate of 1 °C/min. It can be obtained from Figure 2a that the  $\gamma'$  precipitates were fully dissolved into the matrix. When cooling to 1010 °C, as shown in Figure 5a, there are no  $\gamma'$  precipitates in the  $\gamma$  matrix but a few small  $\gamma'$  particles at the grain boundaries. Precipitation of the  $\gamma'$  precipitates at the grain boundaries initially result from the fact that the grain boundaries are the high-speed channels for the diffusion of atoms. These small  $\gamma'$  precipitates were discontinuously distributed and showed spherical morphology whose diameters were about 26 nm. However, as the cooling rate is too fast, there is not enough time for the nucleation of the  $\gamma'$  precipitates. When the temperature of the samples cools to 1000 °C, as is shown in Figure 5b, the fine  $\gamma'$  precipitates were precipitated in the  $\gamma$  matrix, which were continuously distributed and showed spherical morphology. It can also be obtained from Figure 5b that the  $\gamma'$

precipitates precipitated in the  $\gamma$  matrix show high density, which may contribute to the high super-saturation and the spinodal decomposition nature of  $\gamma'$  precipitation, and it requires no driving force [24]. It is interesting that there occasionally appeared irregular  $\gamma'$  precipitates containing the fan-type and flower-like  $\gamma'$  precipitates (see the dotted rectangle and loops in Figure 5b). The fan-type  $\gamma'$  precipitates were considered to be related to the serrated grain boundaries, which will be discussed in Section 3.3. As the cooling process continues, it can be obtained from Figure 5c that the fine  $\gamma'$  precipitates were vanished and the density of flower-like  $\gamma'$  precipitates increases when the temperature is 990 °C. It indicates that the fine  $\gamma'$  precipitates were dissolved with the coarsening of the flower-like  $\gamma'$  precipitates. Compared to 990 °C, the  $\gamma'$  precipitates show no considerable difference but the size of the flower-like  $\gamma'$  precipitates increases when it cools to 980 °C.

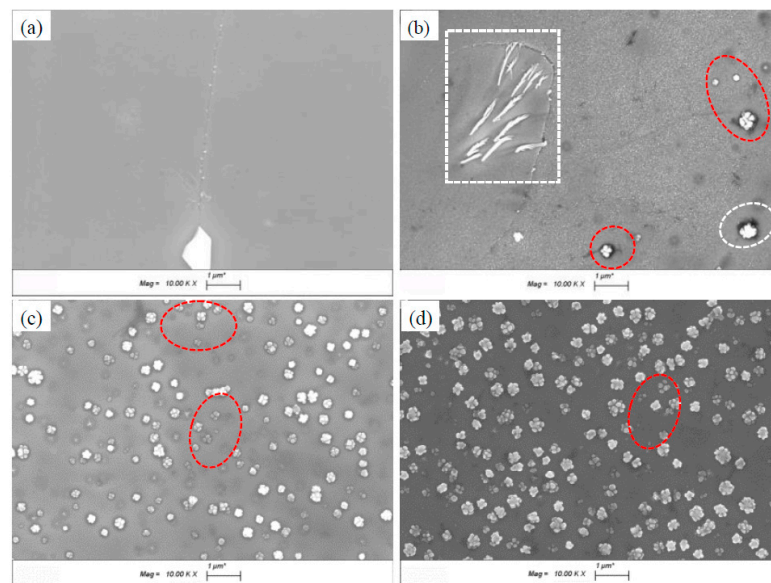


**Figure 5.** The evolution of the  $\gamma'$  precipitates during interrupt cooling at the cooling rate of 1 °C/min: (a) 1010 °C, (b) 1000 °C, (c) 990 °C, (d) 980 °C.

During the whole process, the local aggregation of the similar size of adjacent sphere  $\gamma'$  precipitates was observed (see the red loops in Figure 5) and the outline is similar to the flower-like  $\gamma'$  precipitates, which means that the flower-like  $\gamma'$  precipitates originated from the irregular-shaped clusters of the coarsened  $\gamma'$  precipitates with equivalent sizes. The driving force of the combination coarsening of the  $\gamma'$  precipitates is the trend for the system to reduce the total interfacial energy. With the decrease in the temperature, the several adjacent  $\gamma'$  precipitates continue to integrate and grow, and the flower-like  $\gamma'$  precipitates were obtained (see Figure 5c,d). In addition, it can be noticed that there is a denudation zone of fine precipitates around the  $\gamma'$  cluster which has been coarsened (see Figure 5b), which suggests that the formation of these  $\gamma'$  clusters may be related to the dissolution of small  $\gamma'$  precipitates and solute flux from the small  $\gamma'$  precipitates to the  $\gamma$  matrix, and then diffusion to the larger one.

As we know, the distribution of immobile particles in a solid matrix tends to lower its interfacial free energy by transporting solute atoms from the smaller particles to the larger particles. Therefore, it would diminish the number of the total particles, but this would be accompanied with the increasing of the average particle size. The large particles grow larger while the small one dissolves [25].

Figure 6 sketches the flow of the solute atoms that constitute  $\gamma'$  precipitates during continuous cooling. We suppose that the shaded part is the  $\gamma$  matrix and the circular one is the  $\gamma'$  precipitates, the arrows are the flow direction of the solute atoms. Ostwald ripening is a coarsening process controlled by matrix diffusion, which indicates that the nature

of the coarsening process is that the smaller particles dissolve into the matrix, and then the atoms in the matrix diffuse to the larger particles [14], thereby diminishing the total particle number but increasing the average particle size. In this process, the flow of the solute atoms involve the direction a: dissolve from the small  $\gamma'$  precipitates to the  $\gamma$  matrix, which involves the diminishing of the small particles; direction b: diffuse to the large  $\gamma'$  precipitates from the matrix, which involves the coarsening of the large particles; and direction c: involving the short distance among  $\gamma'$  precipitates close to each other, which would lead to the formation of the flower-like  $\gamma'$  precipitates. It involves the short distance among  $\gamma'$  precipitates close to each other to remove elastically distorted matrix between  $\gamma'$  precipitates, which would lead to the formation of the flower-like  $\gamma'$  precipitates [26].

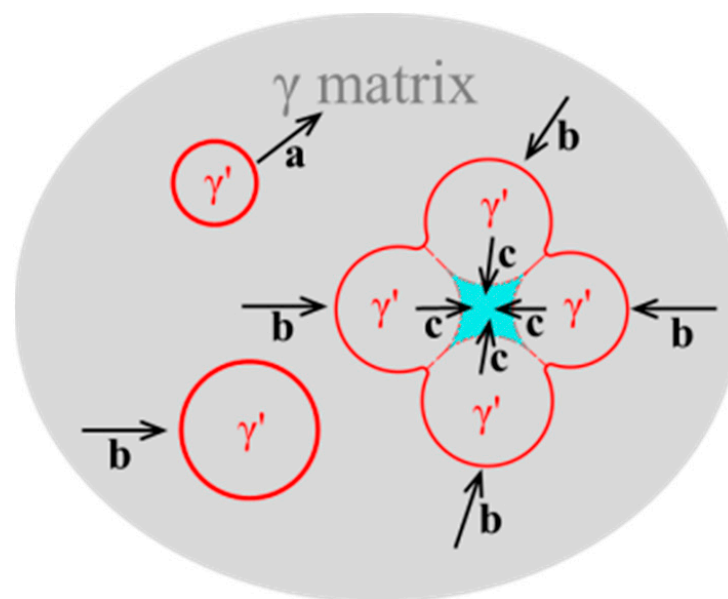


**Figure 6.** Schematic illustration of the flow of the atoms constituting  $\gamma'$  precipitates during continuous cooling.

### 3.3. The Morphology of the Grain Boundaries under Different Cooling Rates

Figure 7 presents the inverse pole figure (IPF) maps under different cooling rates. As we can see from Figure 7a,d, the grain boundaries show flat grain boundaries under water cooling. In addition, fine  $\gamma'$  precipitates were discontinuously distributed at the grain boundaries. However, at the cooling rates of 5 °C/min and 1 °C/min (lower cooling rates), the continuously slow cooling can successfully lead to the serrated grain boundaries (see the black loops in Figure 7b,c). As for the serrated grain boundaries, a number of parameters can be easily recorded from the image of the grain boundary structure. The most common parameters should be the wavelength between successive peaks ( $\lambda$ ) and the maximum amplitude (A) of the serration, which can be approximated by the curve of the sine function. The schematic illustration of geometry parameters of the grain boundary is shown in Figure 8. It can be concluded from Figure 8 that the value of  $\lambda$  and A is larger with the decrease in the cooling rates, which means that the degree of serrated grain boundaries was increased. Specifically, the wavelength between successive peaks is 11.37  $\mu\text{m}$  and the maximum amplitude is 1.16  $\mu\text{m}$  at the cooling rate of 5 °C/min, while the wavelength between successive peaks is 12.65  $\mu\text{m}$  and the maximum amplitude is 2.08  $\mu\text{m}$  at the cooling rate of 1 °C/min, which is caused by the increasing growth of the precipitates on the grain boundary.

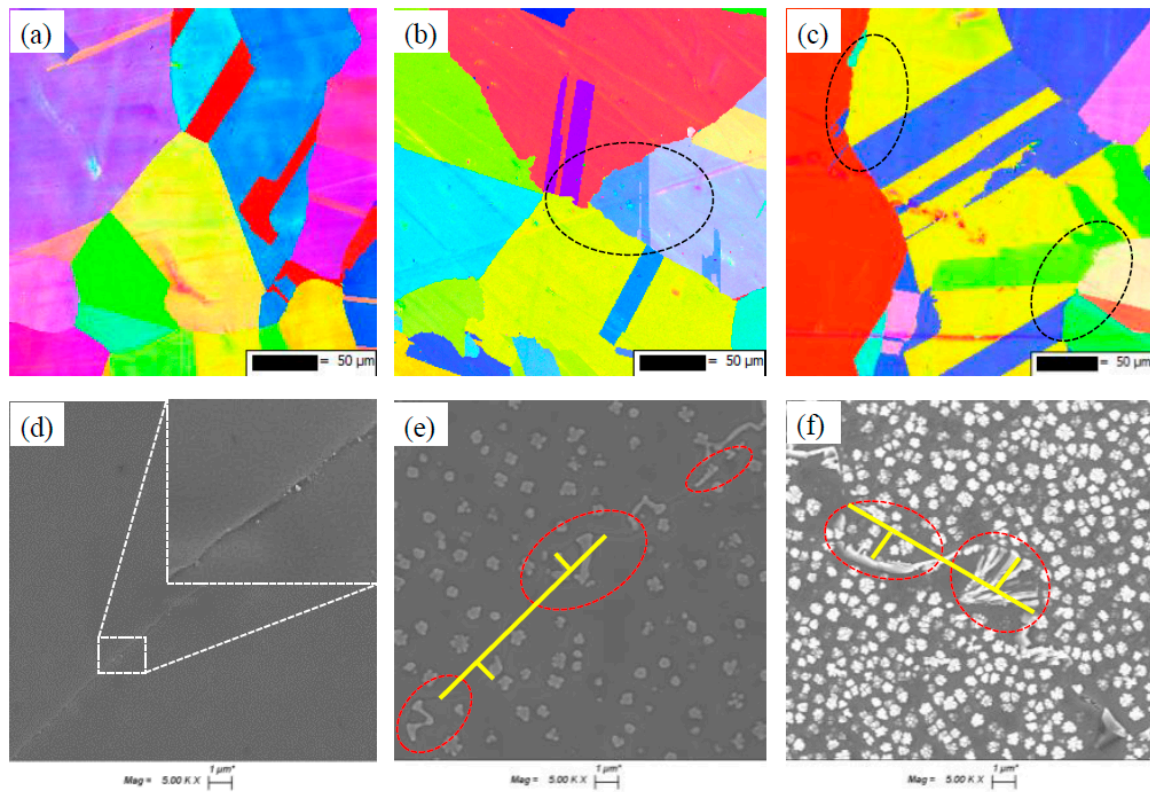


**Figure 7.** The morphology of the grain boundaries under different cooling rates. (a) IPF map at water quench, (b) IPF map at 5 °C/min, (c) IPF map at 1 °C/min, (d) SEM at water quench, (e) SEM at 5 °C/min, (f) SEM at 1 °C/min.

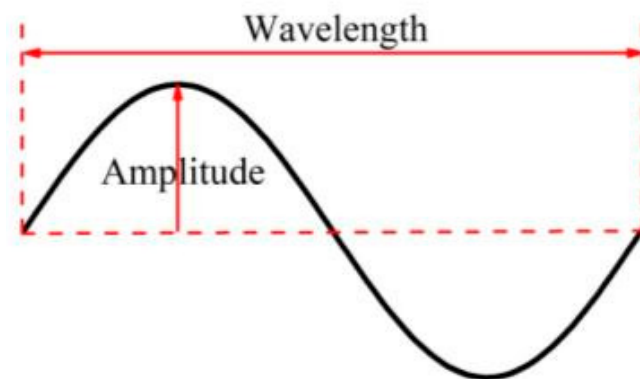


**Figure 8.** Schematic illustration of geometry parameters of the grain boundary.

The serrated grain boundaries originate from the fan-type irregular  $\gamma'$  precipitates and the heterogeneous phases located on the grain boundaries (see the red loops in Figure 7e,f). It can be obtained from Figure 7a that there are no  $\gamma'$  precipitates in the  $\gamma$  matrix and only a small amount of  $M_{23}C_6$  carbides at the grain boundary at water quench. However, as the cooling rate slowed to 5 °C/min, the heterogeneous phases and even the fan-type  $\gamma'$  precipitates started to appear, which can be seen at the curve grain boundaries. At the cooling rate of 1 °C/min, it shows that there are larger heterogeneous phases and fan-type  $\gamma'$  precipitates. In conclusion, the grain boundary serration is caused by the preferential growth of fan-type  $\gamma'$  precipitates along the grain boundary, which means that the grain boundary changes from a flat interface to a convoluted one because of the fan-type  $\gamma'$  precipitates.

Figure 9a–c shows the coincidence site lattice (CSL) maps for the specimens under different cooling rates. Figure 9d presents the quantified frequency of the serrated grain

boundaries, which is expressed in linear density ( $\mu\text{m}/\text{mm}^2$ ). It illustrates from Figure 9d that the linear density of serrated grain boundaries is increasing with the decreasing cooling rates. The higher linear density of serrated grain boundaries with the lower cooling rates may result from the fan-type  $\gamma'$  precipitates and the heterogeneous phases located on the grain boundaries, which is consistent with Hong's [27] research that the coarse and discrete carbides were detected to precipitate at the high-angle grain boundaries.

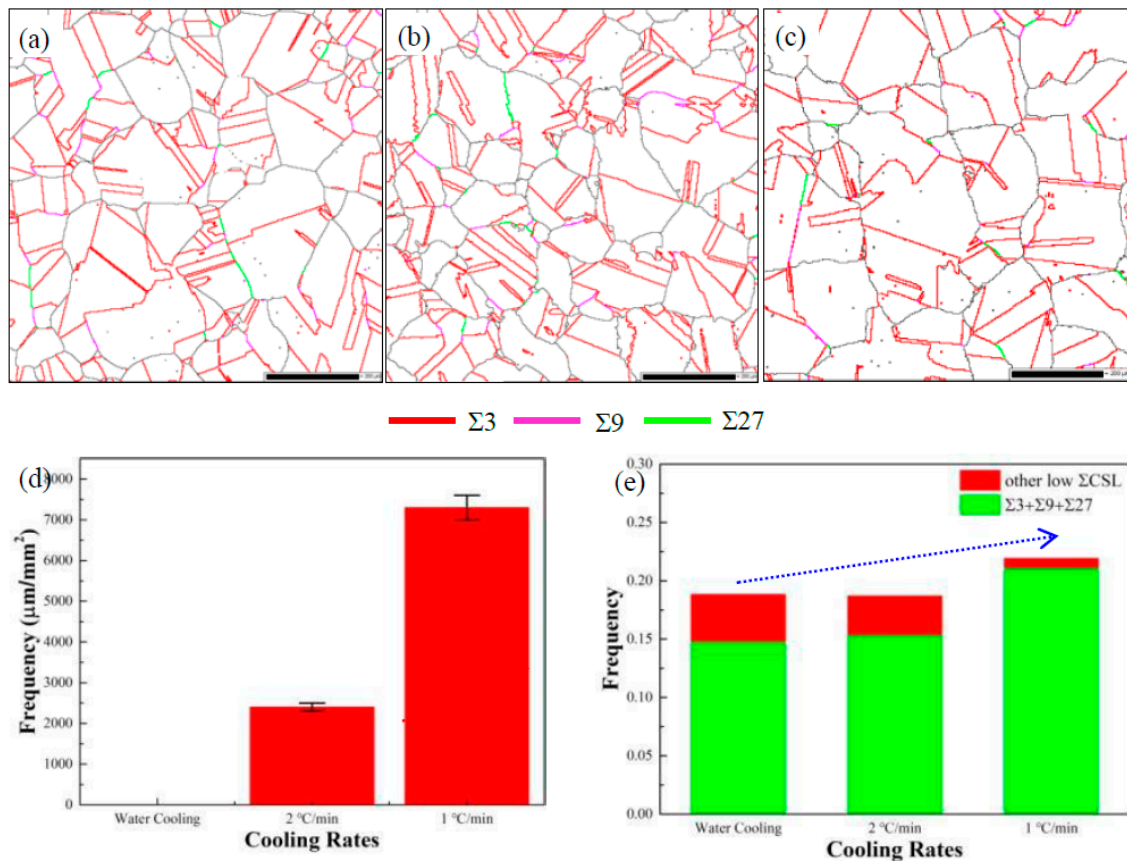


**Figure 9.** CSL maps for the specimens under different cooling rates. (a) Water-quenched, (b) 5 °C/min, (c) 1 °C/min, (d) the frequency of serrated grain boundaries, (e) the frequency of the low  $\Sigma$ CSL boundaries.

Additionally, it can be obtained from Figure 9e that the content of the low  $\Sigma$ CSL boundaries is increasing with the decreasing of the cooling rates. Specifically, the content of low  $\Sigma$ CSL boundaries is 15.23% under water cooling, while 21.2% at the cooling rate of 1 °C/min. According to the theoretical basis of grain boundary engineering, the content of the special grain boundary (generally refers to the low  $\Sigma$ CSL grain boundary with  $\Sigma \leq 29$ ) [28,29] can significantly improve the properties related to the grain boundary, especially the creep property [30–32]. In conclusion, the decreasing cooling rate can increase the content of the low  $\Sigma$ CSL boundaries and thereby enhance the mechanical properties, especially the creep property.

#### 4. Conclusions

This paper presents the evaluation of the  $\gamma'$  precipitates and the grain boundaries under continuous cooling from the subsolvus solution temperature ( $T_{\text{sup}}$ ). The following conclusions can be summarized:

1. The morphology of the  $\gamma'$  precipitates was strongly dependent on the cooling rates; the sphere  $\gamma'$  precipitates were formed under the fast cooling rates, while flower-like ones under the slower cooling rates.

2. The solute atoms that constitute the  $\gamma'$  precipitates may involve the process of dissolution from the small  $\gamma'$  precipitates to the  $\gamma$  matrix, diffusing to the large  $\gamma'$  precipitates from the matrix, and the short distance among  $\gamma'$  precipitates close to each other.
3. The formation of serrated grain boundaries was mainly associated with the presence of fan-type  $\gamma'$  precipitates and the heterogeneous phases located on the grain boundaries. The degree of serration of grain boundaries is more apparent with the decreasing of the cooling rates.
4. The linear density of serrated grain boundaries is increasing with the decreasing cooling rates, and the fraction of overall low  $\Sigma$ CSL grain boundaries was enhanced with the decreasing of the cooling rates which is of benefit in improving the creep property.

**Author Contributions:** Conceptualization, D.L. and H.W. (Haiping Wang); methodology, H.W. (Haiping Wang) and J.W.; software, H.W. (Haiping Wang); validation, J.W. and Y.Y.; formal analysis, H.W. (Haiping Wang); investigation, H.W. (Haiping Wang), H.R. and H.W. (Hai Wang); resources, H.W. (Haiping Wang) and J.N.; data curation, L.W.; writing—original draft preparation, H.W. (Haiping Wang); writing—review and editing, H.W. (Haiping Wang), J.N. and L.W.; visualization, D.L.; supervision, Y.Y.; project administration, D.L.; funding acquisition, J.W. All authors have read and agreed to the published version of the manuscript.

**Funding:** National Natural Science Foundation of China: 52101052; Fundamental Research Funds for the Central Universities: 3102019ZX004; Natural Science Basic Research plan in Shaanxi Province of China: 2020JQ-182; Natural Science Foundation of Chongqing: cstc2020jcyj-msxmX0046.

**Institutional Review Board Statement:** Not applicable.

**Informed Consent Statement:** Not applicable.

**Data Availability Statement:** Not applicable.

**Acknowledgments:** The authors would like to thank for their support the Natural Science Foundation of Chongqing, China (No. cstc2020jcyj-msxmX0046), Natural Science Basic Research plan in Shaanxi Province of China (No. 2020JQ-182), the Fundamental Research Funds for the Central Universities (No. 3102019ZX004), and National Natural Science Foundation of China (No.52101052).

**Conflicts of Interest:** The authors declare no conflict of interest.

## References

1. Fox-Rabinovich, G.S.; Kovalev, A.I.; Aguirre, M.H.; Beake, B.D.; Yamamoto, K.; Veldhuis, S.C.; Endrino, J.L.; Wainstein, D.L.; Rashkovskiy, A.Y. Design and performance of AlTiN and TiAlCrN PVD coatings for machining of hard to cut materials. *Surf. Coatings Technol.* **2009**, *204*, 489–496. [[CrossRef](#)]
2. Chamanfar, A.; Jahazi, M.; Gholipour, J.; Wanjara, P.; Yue, S. Evolution of flow stress and microstructure during isothermal compression of Waspaloy. *Mater. Sci. Eng. A* **2014**, *615*, 497–510. [[CrossRef](#)]
3. Amiri, A.; Bruschi, S.; Sadeghi, M.H.; Bariani, P. Investigation on hot deformation behavior of Waspaloy. *Mater. Sci. Eng. A* **2013**, *562*, 77–82. [[CrossRef](#)]
4. Jia, C.; Zhang, F.; Kang, W.; Lv, S. Effective solution treatment can result in improved creep performance of superalloys. *J. Alloy. Compd.* **2019**, *770*, 166–174. [[CrossRef](#)]
5. Chang, K.M.; Liu, X. Effect of  $\gamma'$  content on the mechanical behavior of the WASPALOY alloy system. *Mater. Sci. Eng. A* **2001**, *308*, 1–8. [[CrossRef](#)]
6. Chamanfar, A.; Jahazi, M.; Gholipour, J.; Wanjara, P.; Yue, S. Mechanical Property and Microstructure of Linear Friction Welded WASPALOY. *Met. Mater. Trans. A* **2011**, *42*, 729–744. [[CrossRef](#)]
7. Zhao, S.Q.; Xie, X.S. Mechanical Properties and Microstructure Evolution of WASPALOY after Long Exposure. *Mater. Mech. Eng.* **2006**, *30*, 62–65.
8. Wang, L.; Yang, G.; Lei, T.; Liu, Q. Microstructure and mechanical properties of waspaloy alloy as steam turbine blade after long-term thermal exposure. *Trans. Mater. Heat Treat.* **2014**, *35*, 60–64.
9. Kelekanjeri, G.; Gerhardt, R.A. Effect of High Temperature Exposure on the Microstructure of Waspaloy. *Microsc. Microanal.* **2004**, *10*, 688–689. [[CrossRef](#)]
10. Hwang, J.Y.; Banerjee, R.; Tiley, J.; Srinivasan, R.; Viswanathan, G.B.; Fraser, H.L. Nanoscale Characterization of Elemental Partitioning between Gamma and Gamma Prime Phases in René 88 DT Nickel-Base Superalloy. *Met. Mater. Trans. A* **2008**, *40*, 24–35. [[CrossRef](#)]
11. Babu, S.S.; Miller, K.M.; Vitek, M.J.; David, S.A. Characterization of the microstructure evolution in a nickel base superalloy during continuous cooling conditions. *Acta Mater.* **2001**, *49*, 4149–4160. [[CrossRef](#)]

12. Sarosi, P.M.; Wang, B.; Simmons, J.P.; Wang, Y.; Mills, M.J. Formation of multimodal size distributions of  $\gamma'$  in a nickel-base superalloy during interrupted continuous cooling. *Scr. Mater.* **2007**, *57*, 767–770. [[CrossRef](#)]
13. Wen, Y.H.; Simmons, J.P.; Shen, C.; Woodward, C.; Wang, Y. Phase-field modeling of bimodal particle size distributions during continuous cooling. *Acta Mater.* **2003**, *51*, 1123–1132. [[CrossRef](#)]
14. Wang, H.; Liu, D.; Shi, Y.; Wang, J.; Qin, W. Matrix-Diffusion-Controlled Coarsening of the  $\gamma'$  Phase in Waspaloy. *Met. Mater. Int.* **2019**, *25*, 1410–1419. [[CrossRef](#)]
15. Wen, Y.H.; Wang, B.; Simmons, J.P.; Wang, Y. A phase-field model for heat treatment applications in Ni-based alloys. *Acta Mater.* **2006**, *54*, 2087–2099. [[CrossRef](#)]
16. Balikci, E.; Raman, A. Characteristics of the  $\gamma'$  precipitates at high temperatures in Ni-base polycrystalline superalloy IN738LC. *J. Mater. Sci.* **2000**, *35*, 3593–3597. [[CrossRef](#)]
17. Arabi, H.; Rastegari, S.; Mirhosseini, M.; Sadeghi, B.M. Effect of cooling rates from partial solution temperature and aging on  $\gamma'$  precipitation in IN792 superalloy. *Mater. Sci. Technol.* **2013**, *29*, 1513–1517. [[CrossRef](#)]
18. Qiu, C.L.; Andrews, P. On the formation of irregular-shaped gamma prime and serrated grain boundaries in a nickel-based superalloy during continuous cooling. *Mater. Charact.* **2013**, *76*, 28–34. [[CrossRef](#)]
19. Doi, M.; Miyazaki, T.; Wakatsuki, T. The effect of elastic interaction energy on the morphology of  $\gamma'$  precipitates in nickel-based alloys. *Mater. Sci. Eng.* **1984**, *67*, 247–253. [[CrossRef](#)]
20. Lee, J.K. Splitting of coherent precipitates caused by elastic non-equilibrium. *Theor. Appl. Fract. Mech.* **2000**, *33*, 207–217. [[CrossRef](#)]
21. Tiley, J.; Viswanathan, G.B.; Hwang, J.Y.; Shiveley, A.; Banerjee, R. Evaluation of gamma prime volume fractions and lattice misfits in a nickel base superalloy using the external standard X-ray diffraction method. *Mater. Sci. Eng. A* **2010**, *528*, 32–36. [[CrossRef](#)]
22. Singh, A.R.P.; Nag, S.; Hwang, J.Y.; Viswanathan, G.B.; Tiley, J.; Srinivasan, R.; Fraser, H.L.; Banerjee, R. Influence of cooling rate on the development of multiple generations of  $\gamma'$  precipitates in a commercial nickel base superalloy. *Mater. Charact.* **2011**, *62*, 878–886. [[CrossRef](#)]
23. Tiley, J.; Viswanathan, G.B.; Srinivasan, R.; Banerjee, R.; Dimiduk, D.M.; Fraser, H.L. Coarsening kinetics of  $\gamma'$  precipitates in the commercial nickel base Superalloy Rene´ 88 DT. *Acta Mater.* **2009**, *57*, 2538–2549. [[CrossRef](#)]
24. Viswanathan, G.B.; Banerjee, R.; Singh, A.; Nag, S.; Tiley, J.; Fraser, H.L. Precipitation of ordered phases in metallic solid solutions: A synergistic clustering and ordering process. *Scr. Mater.* **2011**, *65*, 485–488. [[CrossRef](#)]
25. Picasso, A.; Somoza, A.; Tolley, A. Nucleation, growth and coarsening of  $\gamma'$ -precipitates in a Ni–Cr–Al-based commercial superalloy during artificial aging. *J. Alloys Compd.* **2009**, *479*, 129–133. [[CrossRef](#)]
26. Doherty, R.D. Role of interfaces in kinetics of internal shape changes. *Met. Sci.* **1982**, *16*, 1–14. [[CrossRef](#)]
27. Hong, H.U.; Kim, I.S.; Choi, B.G.; Kim, M.Y.; Jo, C.Y. The effect of grain boundary serration on creep resistance in a wrought nickel-based superalloy. *Mater. Sci. Eng. A* **2009**, *517*, 125–131. [[CrossRef](#)]
28. Randle, N. Twinning-related grain boundary engineering. *Acta Mater.* **2004**, *52*, 4067–4081. [[CrossRef](#)]
29. Kumar, M.; Schwartz, A.J.; King, W.E. Microstructural evolution during grain boundary engineering of low to medium stacking fault energy fcc materials. *Acta Mater.* **2002**, *50*, 2599–2612. [[CrossRef](#)]
30. Yeh, A.-C.; Lu, K.-W.; Kuo, C.-M.; Bor, H.-Y.; Wec, C.-N. Effect of serrated grain boundaries on the creep property of Inconel 718 superalloy. *Mater. Sci. Eng. A* **2011**, *530*, 525–529. [[CrossRef](#)]
31. Hong, H.U.; Jeong, H.W.; Kim, I.S.; Choi, B.G.; Yoo, Y.S.; Jo, C.Y. A Study on the Formation of Serrated Grain Boundaries and Its Applications in Nimonic 263. *Mater. Sci. Forum* **2010**, *638*, 2245–2250. [[CrossRef](#)]
32. Zhao, Y.Q.; Qu, H.L.; Wang, M.M.; Wu, H.; Zhu, K.Y. Thermal stability and creep behavior of Ti–V–Cr burn-resistant alloys. *J. Alloy. Compd.* **2006**, *407*, 118–124. [[CrossRef](#)]